Disclaimer

A Pushered capsule implosion as an alternate approach to the ignition regime for inertial confinement fusion LLNL-JRNL-825074

S.A. MacLaren,[1] D.D.-M. Ho,[1] O.A. Hurricane,[1] E.L. Dewald,[1] D.A. Martinez,[1] R.E. Tipton,[1] J.E. Pino,[1] C.V. Young,[1] H.W. Xu,[2] C. Kong,[2] and K. Sequoia[2]

[1)]*Lawrence Livermore National Laboratory, P.O. Box 808, Livermore, CA 94550*

[2)]*General Atomics, La Jolla, CA 92037*

(*Electronic mail: maclaren2@llnl.gov)

(Dated: 3 March 2022)

In inertial confinement fusion, the threshold for ignition is a highly dynamic quantity as the sources and sinks of power in the hot spot can vary rapidly. In this article, we consider the ignition condition as a race between heating and disassembly rates and make use of a prior solution to the fusion hot-spot thermodynamics to develop a Lawson-like ignition criteria for pressure×confinement time (p-τ) versus temperature. Low-Z capsule designs reach the temperature for this threshold using as much of the shell as feasible as ablator but then are limited in τ by low stagnated mass. An alternate approach, the pushered single shell (PSS) design[1] introduces a dense inner layer of Mo-Be alloy that is smoothly graded outward to pure Be, increasing the confinement time at stagnation and lowering the temperature requirement at the ignition threshold. Here we describe a PSS ignition design for the National Ignition Facility (NIF) and use the theory as well as simulations to compare it with the low-Z capsule approach. Additionally, we show how an adjustment to the design is used to anticipate the effects of mixing at the fuel-ablator interface.

I. INTRODUCTION

In order to gauge progress towards achieving ICF ignition the laboratory, it has been common practice to define ignition metrics for the imploded state against which laboratory results can be compared[2–7]. Many of these ignition metrics are derived following Lawson[8] by equating the rate of energy deposition by the alpha particles from deuterium-tritium fusion reactions to the rate at which energy is lost from the fusing plasma. These frame the ignition criteria as a threshold for the product of hot spot pressure and confinement time (p-τ) and are often referred to as Generalized Lawson Criteria (GLC)[6,9], with the threshold parametrized as p-$\tau(T)$. Physically these criteria represent a threshold for the onset of burn propagation at which the alpha deposition power is sufficient to raise the temperature locally at the boundary of a "hot spot" to cause further fusion reactions, thus expanding the volume of burning plasma. In service of a more measurable definition of ignition, recent studies[6,7] examine the ratio of the neutron yield produced by the implosion in the presence of alpha deposition versus the yield produced by a similar implosion without alpha heating, with the "yield amplification" ratio found to be several tens at the ignition threshold.

The p-$\tau(T)$ form for the GLC highlights the trade-off for a given implosion kinetic energy at stagnation between shell mass remaining (through τ) and implosion peak velocity (through T). Low-Z materials make for efficient ablators, and this choice for the capsule shell generally drives this trade-off towards higher velocity at the expense of stagnated mass. Indeed, the highest performing laboratory implosions to date use CH or pure C for the capsule shell[10,11] and typically retain only a very small fraction (2∼3%) of the initial shell as stagnated mass to participate in confinement. However, higher velocities tend to increase Raleigh-Taylor instability growth in ICF capsules[12] through greater acceleration and deceleration. In fact, experimental evidence suggests a cliff in ICF implosion performance due to a loss in confinement that is proportional to a high power of velocity[10,13]. The potential hazards of high velocity motivate a consideration of lower-velocity designs, where, as we shall show, the additional stagnated mass permits access to the ignition threshold at lower temperature.

II. DEVELOPMENT OF THE IGNITION METRIC

We posit that the ignition threshold can be thought of as a competition between the static heating rate and the disassembly rate. We begin our analysis, which closely follows that of Reference 7, by examining the time derivative of the internal energy ($E_{hs} = mc_{DT}T$) of an ignition hotspot:

$$\frac{dE_{hs}}{dt} = c_{DT}\left(T\frac{dm}{dt} + m\frac{dT}{dt}\right) \tag{1}$$

where T is the hotspot temperature, m the hotspot mass and $c_{DT} = 0.115$ GJ/(g·keV) is the heat capacity of equi-molar deuterium-tritium fuel. The time derivatives of the hotspot temperature and mass are described by:

$$c_{DT}\frac{dT}{dt} = f_\alpha Q_\alpha - f_B Q_B - Q_e - \frac{1}{m}p\frac{dV}{dt} \tag{2}$$

$$\frac{dm}{dt} = \frac{m}{c_{DT}T}[Q_\alpha(1-f_\alpha) + Q_e] \tag{3}$$

where Q_α is the heating rate per unit mass from DT fusion alpha particles, Q_B is the radiated power per unit mass from the hotspot due to bremsstrahlung x-rays, and Q_e is the power per unit mass lost at the hot spot boundary due to electron thermal conduction. f_α represents the fraction of alpha particles from DT fusion that deposit their energy in the hot spot and f_B the fraction of the radiation from DT fusion that escapes the hotspot (f_B may be < 1 if the hotspot is not optically thin to the

bremsstrahlung x-rays). Equation 2 represents the dynamic power balance per unit mass of the hotspot under the assumption that there are no sources or sinks other than alpha heating, electron thermal conduction, radiation and pdV work. Equation 3 represents the assumptions that in a cryogenic-layered fuel implosion, some losses at the boundary with the cold fuel are "recycled" into hot spot mass, namely alpha particles and electron heat conduction. In particular, the first term on the right hand side of Equation 3 simply states that the fraction of alphas not absorbed in the hot spot $(1-f_\alpha)$ will be absorbed in the inner layer of cold fuel, converting that cold fuel mass into additional hot spot mass. This assumption is valid for the case in which the alphas have a very short range (2∼3 μm) in the dense fuel just outside the hot spot, consistent with modern calculations of alpha stopping[14]. The assumption is quite useful in what follows at it removes f_α and therefore its dependence on temperature and hotspot areal density from the hotspot heating rate.

Combining equations 1-3 we write an expression for the net hotspot heating rate:

$$\frac{\dot{E}_{hs}}{E_{hs}} = \frac{Q_\alpha - f_B Q_B}{c_{DT} T} - \frac{p_{hs}}{E_{hs}}\frac{dV}{dt} = p_{hs}F(T) - \frac{p_{hs}}{E_{hs}}\frac{dV}{dt} \quad (4)$$

where considering the hotspot density $\rho_{hs} = \frac{3}{2}\frac{p_{hs}}{c_{DT}T}$,

$$F(T) = \frac{3}{2}\frac{Q_\alpha - f_B Q_B}{\rho_{hs}(c_{DT}T)^2}. \quad (5)$$

Here $Q_\alpha = 8.2\times10^{24}\rho\langle\sigma v\rangle$, $Q_B = 3.1\times10^{7}\rho\sqrt{T}$, both in units of GJ/(g·s), and $\langle\sigma v\rangle$ is the D-T reaction rate per unit volume as a function of temperature[15]. Following Reference 16, we will use a fit to equation 5 to produce a form for $F(T)$ in units of cm^3/(GJ·s) that is closely matched to that using the Reference 15 value of $\langle\sigma v\rangle$ in the range of $2 < T < 10$ KeV:

$$F(T) \approx [4.7 + 11 f_B + (0.4 + 0.86 f_B)T]\ln\left(\frac{T}{4.3 f_B^{0.3}}\right)\times 10^8 \quad (6)$$

Note that if the temperature is less than $4.3 f_B^{0.3}$ keV, $F(T) < 0$. This simply is a statement of the minimum temperature for a positive static hot spot power balance in the absence of PdV work.

Two processes, alpha heating and pdV work, have the potential to add energy to the hotspot and serve to increase hotspot temperature leading up to minimum volume. However at minimum volume the pdV work becomes a loss term, and the hotspot will only continue to heat as long as the alpha heating power continues to exceed the power lost due to pdV expansion and radiation. Thus, the approach to ignition can be thought of as a "race" between the static heating rate and dynamic disassembly rate, characterized by the two terms on the right hand side of equation 4. For implosions nearing the ignition threshold, the alpha heating will exceed the losses for some time after the start of the expansion, and the critical "bootstrap" time to consider when defining this threshold is therefore the period from the onset of stagnation to the peak rate of fusion energy production[6]. Figure 1 illustrates this phenomena by plotting the fusion energy production rate

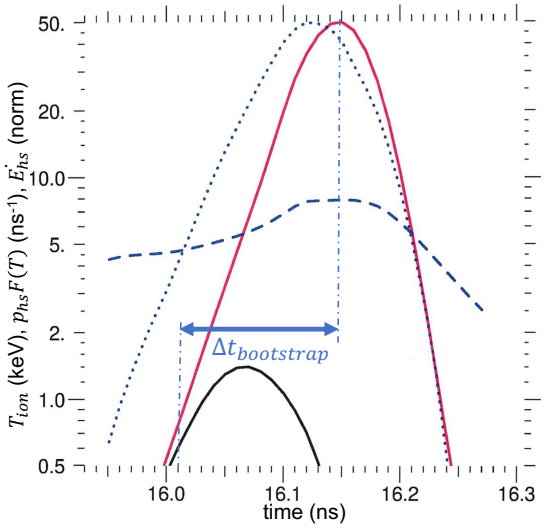

FIG. 1. Fusion energy production rate for an implosion simulation without (black) and with (red) alpha deposition. Also plotted are the burn-weighted ion temperature (dashed) and the static heating rate $p_{hs}F(T)$ from equation 4 (dotted). $\Delta t_{bootstrap}$ is the period from the beginning of the no-alpha burn-width until the peak energy production for the simulation with alpha deposition and represents the time during which the heating rate must exceed the disassembly rate in order to achieve significant yield amplification.

for a 1D LASNEX[17] simulation of a "High-Foot"[18] CH implosion performed at the National Ignition Facility[19,20] (NIF) together with that of the same simulation run without allowing alpha particles to deposit energy. The ratio of the integrals of the two curves is therefore the yield amplification due to alpha heating (∼ 23 in this case), and the bootstrap time is the period from the beginning of the no-alpha burn-width until the peak energy production for the simulation with alpha deposition. Also plotted are the static heating rate term $pF(T)$ from equation 4 and the burn-weighted ion temperature. For this analysis, we wish to find the average static heating rate

$$\langle p_{hs}F(T)\rangle = \frac{\int_0^{t_{max}} p_{hs}F(T)dt}{\Delta t_{bootstrap}} = \frac{p_{hs}H(T_0)\sqrt{\frac{T}{\bar{T}}}}{\Delta t_{bootstrap}} \approx p_{hs}H(T_0) \quad (7)$$

where

$$H(T_0) = \frac{\sqrt{\pi}F(T_0)}{\sqrt{\frac{2\gamma}{\gamma-1} + \frac{2T_0}{F(T_0)}\frac{\partial F}{\partial T}\big|_{T_0}}}. \quad (8)$$

Here T_0 corresponds to the peak temperature, and again following Reference 7 the polytropic index $\gamma = 5/3$ comes from the adiabatic assumption for the pressure approaching stagnation. The simulation results plotted in figure 1 indicate that $\Delta t_{bootstrap}$ is consistent with the characteristic rise time of the ion temperature, $\tau_{BW} \equiv \sqrt{\frac{T}{\dot{T}}}$ used in Reference 16 to perform the integration in equation 7 by the method of "steepest decent". We note from Figure 1 that $p_{hs}F(T)$ is nearly as

peaked as the fusion rate, consistent with the assumptions for this method.

Next, we examine the pdV work term in equation 4 in order to derive a disassembly rate. Precisely at stagnation $dV/dt = 0$, but we wish to examine the behavior of disassembly so we expand about minimum volume:

$$\frac{p_{hs}}{E_{hs}}\frac{dV}{dt} = \frac{2}{3V}\frac{d^2V}{dt^2}(t-t_{min}) = \frac{2}{3V}\left[\int (R^2\ddot{R} - 2R\dot{R}^2)d\Omega\right](t-t_{min}) \quad (9)$$

where R is the hot spot radius and the $2R\dot{R}^2$ term in the integral represents residual shell velocity which is only non-zero in the case of 2D or 3D shape asymmetry; we will neglect it for this 1D analysis. Here we note that the deceleration is related to the force exerted by the stagnating hot spot across the stagnation shock through Newton's second law[13]:

$$\ddot{R}_{hs} = \frac{4\pi R_{hs}^2 p_{hs}}{M_{stag}} \quad (10)$$

and we identify $2(t-t_{min})$ as the confinement time, which can also be written in terms of the stagnated mass M_{stag}[9]:

$$2(t-t_{min}) = \tau_{conf} \approx \sqrt{\frac{M_{stag}}{p_{hs}4\pi R_{hs}}} \quad (11)$$

Finally, we can use equations 7, 9, 10 and 11 to re-write equation 4, the net heating rate, as:

$$\frac{\dot{E}_{hs}}{E_{hs}} = p_{hs}H(T_0) - \left[\frac{p_{hs}4\pi R_{hs}}{M_{stag}}\right]\tau_{conf} \approx p_{hs}H(T_0) - \frac{1}{\tau_{conf}} \quad (12)$$

Our original ansatz, that to cross the threshold for thermonuclear ignition the static heating rate should be greater than the disassembly rate, then becomes:

$$p_{hs}H(T_0) > \frac{1}{\tau_{conf}} \quad \text{or} \quad p_{hs}\tau_{conf}H(T_0) > 1. \quad (13)$$

We find two important consequences from the ignition criteria described by equation 13. First, together with equation 11, equation 13 implies that for similar hot spot radii and pressure near the ignition threshold, the criteria is proportional to the square root of the stagnated mass. Next, we note that References 7 and 16 obtain a condition very similar to equation 13 but with τ_{conf} replaced by τ_{BW} and the thermodynamic consequence that when this criteria is met, pressure is increasing even as the hot spot volume is also increasing. In principle, the experimentally determined τ_{BW} should be well approximated by the dynamic confinement time τ_{conf}, but experimental confirmation of this is still an outstanding question.

III. DESIGN OF THE PUSHERED SINGLE SHELL PLATFORM

The relationship between stagnated mass and the ignition metric developed in the previous section has important implications for ICF design, and the design of the Pushered Single Shell (PSS) capsule[1,21,22] seeks to take direct advantage. The capsule design is illustrated in Figures 2(a) and (b). In particular, in this design the ablator shell is graded from pure beryllium to a mixture of beryllium and molybdenum. A density gradient in the ablator helps stabilize an otherwise classically unstable interface against Rayleigh-Taylor growth[23], and the shape of the concentration/density gradient for this point design, shown in Figure 2(b), has been carefully constructed to significantly improve implosion stability over a discrete transition to a dense inner layer. A 30 μm layer of 0.9% Mo immediately outside of the graded section minimizes the amount of the graded layer that is ablated, increasing the mass remaining at stagnation. A 4 μm layer of pure Be is included inside the Mo layer to improve stability by placing a low preheat layer next to the fuel[24]. Simulations resolving the measured capsule surface roughness at high mode demonstrate the graded PSS capsule point design with this additional Be layer significantly reduces fuel-ablator mixing over designs with steeper gradients or without the extra Be layer. These instability calculations as well as a detailed description of how the density profile shown in Fig. 2 is obtained will be described in a forthcoming publication[25], while additional design considerations in anticipation of some amount of fuel-ablator mixing are discussed below.

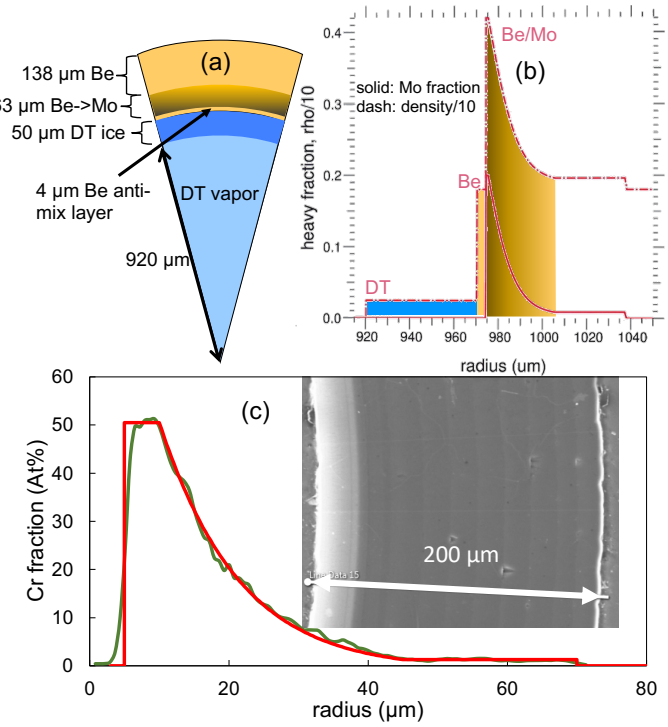

FIG. 2. (a) Schematic of the PSS capsule design[1]. (b) Detail of the Mo density and concentration gradient. (c) For the Be/Cr capsule, the requested (red) Cr concentration is compared with one extracted from a Monte Carlo simulation of energy-dispersive x-ray spectroscopy across the polished shell cross-section (green), with a scanning electron microscopy image of the shell cross-section inset.

PSS capsules using beryllium graded with chromium to achieve a similar density profile have been successfully fab-

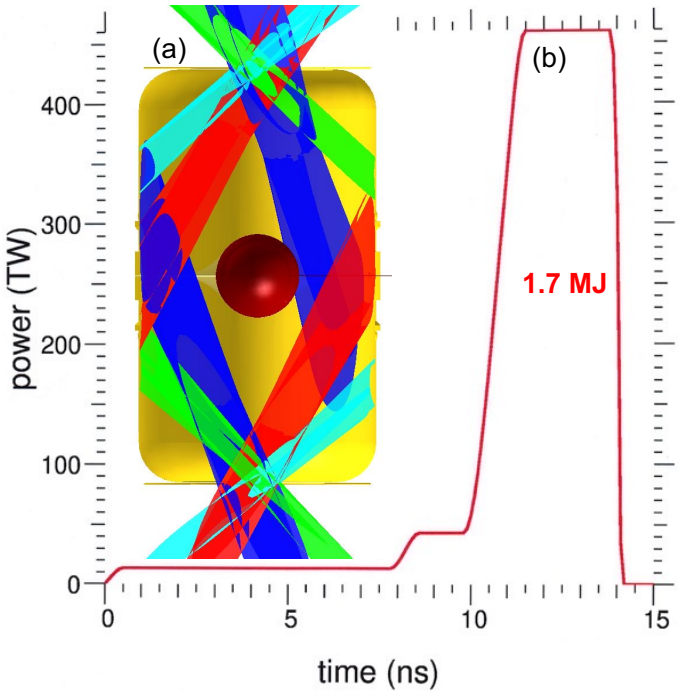

FIG. 3. (a) Geometry of the hohlraum and laser cone configuration used to simulate the x-ray drive for the PSS implosion design. The red and blue beams comprise the "inner cone" while the green and cyan beams comprise the "outer cone". (b) Total NIF laser power vs. time delivered to the hohlraum for the PSS implosion.

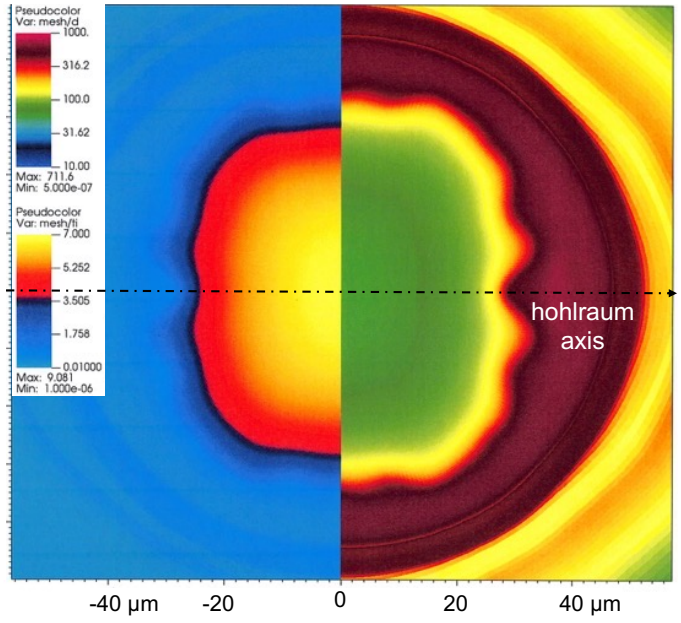

FIG. 4. Plot of ion temperature and density at minimum volume from the integrated laser-hohlraum radiation-hydrodyamics simulation of the PSS implosion.

ricated, and initial implosion experiments on the NIF provide evidence of the efficacy of the graded density scheme. Figure 2(c) demonstrates how a close match to the requested density profile (in red) can be attained in practice (green). These Be-Cr capsules have been filled with high-pressure deuterium and tritium gas and tested in implosion experiments. Details of these capsules and experimental results will be described also in forthcoming publications[26].

The NIF PSS capsule is imploded by x-ray ablation from a laser driven hohlraum. The walls of the hohlraum are made from depleted uranium coated by a very thin (<1 μm) layer of gold. The geometry of the hohlraum is shown in figure 3 together with the NIF laser power history used to generate the x-ray drive. The figure provides representations of the NIF laser "cone" geometry, which consists of azimuthally distributed groups of beams at 23°(blue), 30°(red), 44.5°(green) and 50°(cyan) relative to the vertical axis[20]. The total energy used in the PSS platform design laser pulse is 1.7 MJ. This 3-shock pulse increases the ablation pressure in discrete steps so as to minimize the entropy added to the cryogenic fuel layer. The power profile is designed with the capsule thickness in mind such that the three shocks remain separated from each other as they transit the PSS capsule, including the cryogenic fuel layer, merging only once they break into the vapor in the interior of the capsule.

The hohlraum contains a low density (0.225 mg/cc) He fill to partially tamp the hohlraum wall motion during the pulse, which would otherwise interfere with laser propagation. This low density fill is a compromise between suppressing the wall motion and minimizing stimulated Raman scattering of the incident laser light away from the laser entrance hole[27]. Simulations show that the partially tamped wall motion eventually interferes with the inner (23°and 30°) laser cones, causing the implosion to tend toward an oblate shape due to insufficient drive over the capsule waist. Thus, the PSS hohlraum design also employs cross-beam energy transfer (CBET) to compensate for this deficiency in inner beam propagation by transferring additional power to the inner cones. This has been accomplished in PSS implosions on the NIF to-date by introducing a small separation between the laser wavelength of the inner and outer cone beams[28]. Two-dimensional integrated laser-hohlraum LASNEX simulations that incorporate this CBET effect have been used to successfully model the these implosions; the same model is used to calculate the implosion symmetry for the cryo-layered design presented here. Figure 4 shows the density and ion temperature profiles at minimum volume from this calculation of the PSS implosion that employs a 2.5Å separation between inner and outer cones to achieve symmetry. The low-mode behavior of the implosion is controlled sufficiently well such that the areal density of the shell along any azimuth exceeds 1 gm/cm^2, and the yield of the 2D simulation (4.0×10^{16} 13-15 MeV neutrons) is within 20% of the yield from a 1D simulation using the equivalent x-ray drive.

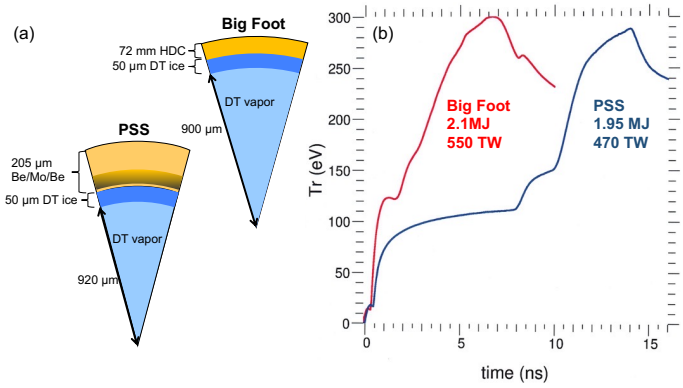

FIG. 5. (a) Comparison of the PSS and pure carbon "BigFoot" capsule designs (b) Radiation temperature histories used to drive the PSS and BigFoot capsules for the simulation comparisons.

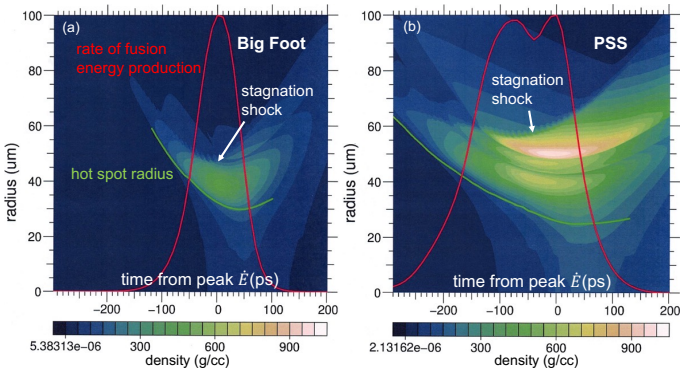

FIG. 6. Comparison of density as a function of radius and time between (a) the pure carbon ablator "Big Foot" and (b) the PSS implosions. In both (a) and (b) the density color scale is linear with a maximum of 1000 g/cc, and the hot-spot boundary and the normalized rate of fusion energy production are the green and red curves, respectively.

IV. COMPARISON OF PSS AND LOW-Z CAPSULE IMPLOSIONS

To illustrate the dramatic difference at stagnation, we make a detailed comparison of 1D implosion dynamics between a PSS implosion and that of a typical high-density carbon ablator as represented by the "Big Foot"[29] capsule. Figure 5(a) compares the PSS capsule with that of the pure carbon "Big Foot" design, and figure 5(b) overplots the hohlraum radiation temperature histories used to drive each implosion. Each drive was chosen such that the corresponding implosion achieves a yield amplfication of ~ 25; the Big Foot hohlraum drive was calculated from a 2.1 MJ, 550 TW laser pulse, and the PSS hohlraum drive from a 1.95 MJ, 470 TW laser pulse. We note that current facility limitations for the NIF cap the total laser pulse energy at 2.0 MJ and the peak laser power at 500 TW. Thus the PSS platform represents a feasible path to achieve significant yield amplification within the current NIF operating limits.

In general, the thinner HDC shell of the Big Foot design allows for a shorter overall laser pulse, which in general is easier for symmetry control. However, the PSS pulse does not include a high power "picket" at the beginning of the pulse which has a tendency to exacerbate symmetry problems due to the enhanced inward radial velocity of the ablated hohlraum wall[30]. The absence of the "picket" in the pulse combined with the aforementioned wavelength separation results in a symmetric implosion in an integrated laser-hohlraum LASNEX simulation including CBET, as shown in figure 4.

Figure 6 compares the density history as a function of radius for the Big Foot versus the PSS implosions for two 1D simulations. The pair of simulations in figure 6 do not include alpha particle deposition; however, when alpha particle deposition is included, these simulations achieve similar yield amplifications ~ 25. Over-plotted in the figure is the energy production rate during stagnation to illustrate the burn duration. An important metric for comparison is the ratio of the masses inside the stagnation shock at minimum volume for the PSS implosion to that of the BigFoot implosion: 3.8 (the ratio of the total ρRs at stagnation is 2.5). The boundary of the stagnated mass is determined by the outgoing stagnation shock, which is clearly delineated in the density color maps. The burn-weighted pressures at stagnation for these two simulations are nearly equal at 360 Gbar. Taking into account the hot-spot radii, equation 11 predicts the ratio of the confinement times to be 2.0, consistent with the ratio of the FWHM of the burn histories (figure 6 red curves) of 2.2.

Equation 13 predicts that the significant increase in confinement time for the PSS implosion will reduce the temperature at which the ignition threshold is reached. To test this conclusion, a series of 1D LASNEX simulations are run for the PSS implosion as well as analogous series of implosions using low-Z ablators: pure carbon (the Big Foot design from figure 6), plastic (the High Foot[18] design), and a beryllium design using 1-3% Cu dopant[31]. For each type of capsule, the series of points is obtained by incrementally increasing the energy of the NIF laser drive, resulting in corresponding incremental increases in peak hohlraum radiation temperatures. Figure 7(a) plots $1/H(T)$ from equation 8 together with points that represent pairs of implosions from each series of simulations. Each point uses p_{hs}-τ from a simulation that does not permit alpha-deposition together with the peak burn-weighted ion temperature from the identical simulation run with alpha-deposition. For implosion pairs in which the yield amplification (ratio of alpha-on to no-alpha simulation yields) is > 20 the markers are changed from circles to squares. The simulations shown in figure 6 for the PSS and Big Foot implosions are represented by the black squares in their respective series closest to (just exceeding) the $GLC = 1$ threshold. The PSS series is noteworthy as it is able to reach the ignition condition at a much lower temperature, using less NIF laser power and energy, and using an implosion with a significantly reduced velocity: 305 km/s vs 380-410 km/s for the low-Z ablators.

To check that equation 13 corresponds to significant ($\sim 20-30\times$) yield amplification, figure 7(b) plots the yield amplification for each 1D simulation series as a function of $GLC = p_{hs}\tau H(T)$. We find that independent of the capsule design and laser pulse shape, each implosion series reaches

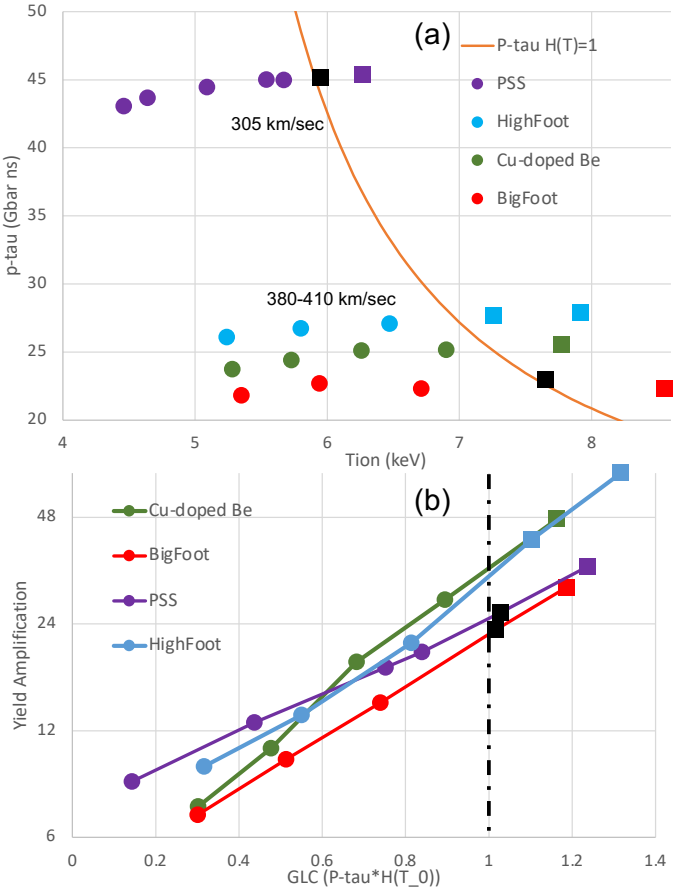

FIG. 7. (a)The equation 13 ignition threshold plotted as p-$\tau(T)$, together with 1D simulations of four different classes (as referenced in the text) of implosions that cross the threshold. (b)Yield amplifications for the same four series of simulations showing similar yield amplifications as the threshold (GLC=1) is reached. For implosion pairs in which the yield amplification (ratio of alpha-on to no-alpha simulation yields) is > 20 the markers are changed from circles to squares. The pair of black squares corresponds to the simulations shown in figure 6.

a yield amplification between 23 and 33 as it crosses the $GLC = 1$ threshold of equation 13.

V. DESIGN CONSIDERATIONS ANTICIPATING FUEL-ABLATOR MIX

The 305 km/s PSS capsule point design described above highlights the fundamental differences between the PSS and low-Z ablator implosions as seen in Figure 7(a), i.e. the ability to reach $GLC > 1$ at peak burn-weighted hot spot temperatures ~ 6 keV. However, mixing between the fuel and shell has the potential to reduce the temperature further through both radiative cooling and lack of compression, resulting in a significant reduction in performance. Based on both simulations[25] and recent data[26], a degradation in performance from fuel-ablator mixing is expected in the PSS implosions. It is important to take this degradation mechanism into account in any design

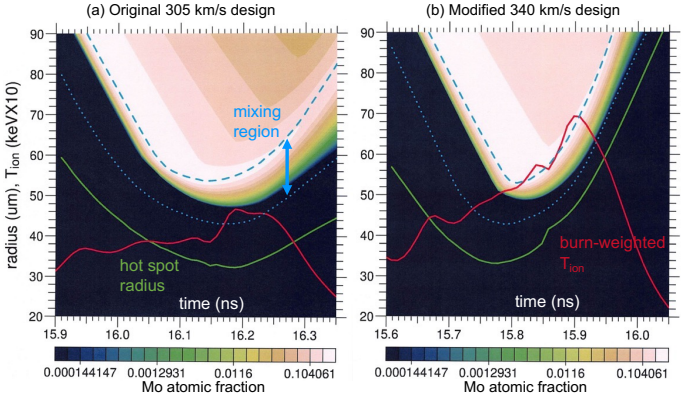

FIG. 8. Mo concentration is plotted as a function of radius and time from peak fusion yield for 1D PSS implosion simulations including the buoyancy-drag model for fuel ablator mixing of (a) the 305 km/s design, and (b) the 340 km/s design. The colors are contours of Mo concentration from 0 to 15% on a log scale. The green curve indicates the hot-spot boundary, and the red curve is the burn-weighted ion temperature $\times 10$. The dashed and dotted blue lines show the radial extent of the mixing region.

put forward for laboratory ICF experiments.

By applying a buoyancy-drag model[31,32] for mixing at the fuel-ablator interface to the 1D LASNEX simulations, we can estimate the degradation for a given PSS implosion. For this application, the model parameters have been calibrated against the results of non-cryo layered PSS implosions on the NIF[26]. We note that the highest performing PSS implosion shown in figure 7 uses an x-ray drive corresponding to 1.95 MJ delivered into the hohlraum shown in figure 3, essentially the maximum capability of the NIF laser. Without mix, the simulations calculate a GLC of 1.24 and a yield amplification of 34; however, addition of the mix model reduces the burn-averaged hot-spot temperature from 6.02 keV to 3.68 keV, and the yield amplification to 3.

To hedge against the effects of fuel-ablator mix and improve the chances of the laboratory PSS implosion reaching $GLC > 1$, we modify the PSS capsule design by trading some of the stagnated mass for peak velocity. We find that by eliminating the 0.9% Mo layer outside the graded layer (as was present in figure 2(b)), the peak fuel velocity increases from 305 to 340 km/s. This increase in velocity is predicted by the simulations to increase the temperature at stagnation enough to overcome fuel-ablator mix and allow for significant yield amplification. Figure 8 compares the Mo concentration as a function of radius and time from peak fusion yield for a pair of implosions driven by the same laser pulse. Both implosions are driven with the same 1.95 MJ laser pulse and are simulated with the same buoyancy-drag mix model parameters. In figure 8(a) we see that for the original design, the incursion of ablator material into the fuel prevents the instantaneous burn-weighted temperature of the hot spot from reaching 5 kV during the stagnation, while figure 8(b) demonstrates how the increased implosion velocity of the revised design results in an increased and rising instantaneous burn-weighted temperature approaching minimum volume which is sufficient to

overcome the additional cooling effects of the mix. Note that in both cases the 1D simulations predict that the combination of the 4 μm pure Be layer together with the cold DT fuel layer ultimately prevents Mo from reaching the hot spot and that the source of degradation is lack of compression of the cold fuel.

High mode simulations such as those referred to in Section III have been performed to examine the stability of this faster implosion[25] and are in rough agreement as to the performance degradation due to fuel-ablator mix with the buoyancy-drag simulations described in this Section. The 340 km/s peak fuel velocity is still significantly lower than, for example, the 380 km/s limit above which a degradation in performance was observed for the CH High Foot implosions[33]. The shell ρR at stagnation for the PSS implosion is 0.8 g/cm^2 compared with 0.2 g/cm^2 as calculated for the High Foot, further insulating the PSS implosion from the failure mode believed to have capped the performance of the High Foot experiments[10]. Ultimately, however, experimental data is needed for the PSS implosion in order to determine if this revised design has sufficient velocity margin to overcome the predicted degradation due to mix. Should experiments show that the mix is more severe than predicted, the research and development of the capsule coating technology indicates capsules can be readily fabricated with reduced peak Mo density. This both increases the density gradient scale length as well as the implosion velocity at some reduction to the tamping. The flexibility demonstrated in fabricating the density profile to specification allows for a significant enhancement of the possible design space for implosions that can overcome the effects of mix and reach the ignition threshold.

Figure 9(a) illustrates the difference in the Mo concentration and density profiles between the original 305 km/s and the revised 340 km/s capsule designs used in the simulations in figure 8. Figure 9(b) once again plots series of 1D LASNEX simulation pairs in the space of $p_{hs}\tau$ vs. T, together with the $GLC = 1$ curve. At high $p_{hs}\tau$ are plotted the results from the original 305 km/s PSS capsule design from figure 7 calculated without a model for fuel-ablator mix. Added to the plot are simulation pairs using the 340 km/s PSS capsule design profile shown by the blue and green points in figure 9(a) calculated with and without mix. Note that the mix simulations of the original 305 km/s design would be too low in temperature to appear on the plot. For the original design as well as the revised design mix cases, the NIF laser energy used to drive the implosions spans the range from 1.7 MJ to 1.95 MJ, while the revised design clean simulations require only 1.8 MJ drive to cross the $GLC = 1$ threshold. Further 1D simulations show that in the absence of mix, the yield amplification of the original design with its greater stagnated mass quickly exceeds that of the revised design once the laser drive is allowed to increase > 2 MJ. But once the practical constraints of the NIF laser together with the expected (from simulations and data) degradation due to mix are taken into account, figure 9(b) shows that the revised design simulations very nearly reach the $GLC = 1$ threshold. Thus the faster revised design represents a hedge against both NIF drive and predicted fuel-ablator mix limitations by trading some of the original stagnated mass for implosion velocity.

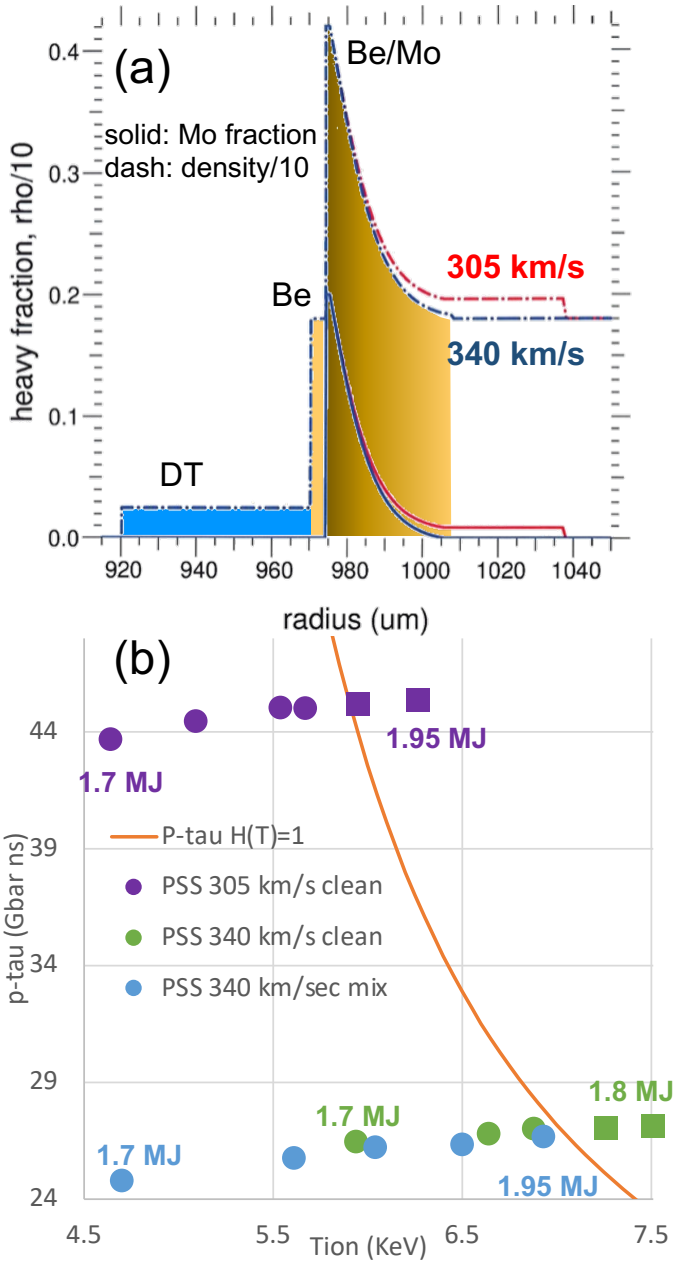

FIG. 9. (a) Comparison of the 305 and 340 km/s PSS capsule design shell profiles, and (b) the results of 1D simulation pairs for both designs with and without mix relative to the $GLC = 1$ curve. In (b), the labels indicate the range of NIF laser energies used for the 1D simulation pairs. Note that the mix simulations of the original 305 km/s design would be too low in temperature to appear on the plot.

VI. CONCLUSIONS

By considering the ignition threshold as a race between heating and disassembly rates, one arrives naturally at a Lawson-like criteria for the ignition threshold. In the space of $p_{hs}\tau$ vs. T, this criteria clearly highlights the difference in approach to the ignition threshold for the PSS as opposed to low-Z ablator implosions. By shifting the balance of velocity

versus mass in the implosion kinetic energy, the PSS platform design accesses the ignition regime at a lower temperature, and at a velocity less likely to push the implosion towards instability. The PSS designs described in this manuscript leverage recent advances in capsule fabrication technology as well as state-of-the-art methodology for achieving symmetric indirect-drive implosions on the NIF. Additionally, the point design for experiments scheduled in 2022 anticipates some amount of fuel-ablator mix in order to reach GLC ~ 1 within the current NIF operating limits, but still at a significantly lower velocity than low-Z capsule implosions to-date. Thus the PSS platform design shows a promising approach to ignition in the near term that may circumvent key obstacles currently limiting the performance of low-Z capsule designs.

The authors wish to thank M. Rosen for several very useful discussions on the topic of the ignition threshold.

This work was performed under the auspices of the U.S. Department of Energy by Lawrence Livermore National Laboratory under contract DE-AC52-07NA27344 and by General Atomics under contract 89233119CNA000063.

[1] D. D.-M. Ho, S. MacLaren, and Y. Wang, "High-yield implosions via radiation trapping and high rho-r," (2018), presented at the 60th Annual Meeting of the APS Division of Plasma Physics, http://meetings.aps.org/link/BAPS.2018.DPP.PO6.11.

[2] C. D. Zhou and R. Betti, "A measurable Lawson criterion and hydro-equivalent curves for inertial confinement fusion," Physics of Plasmas **15**, 102707 (2008), https://doi.org/10.1063/1.2998604.

[3] S. Haan, J. Lindl, D. Callahan, D. Clark, J. Salmonson, B. Hammel, L. Atherton, R. Cook, M. Edwards, S. Glenzer, *et al.*, "Point design targets, specifications, and requirements for the 2010 Ignition Campaign on the National Ignition Facility," Phys. Plasmas **18**, 051001 (2011).

[4] B. K. Spears, S. Glenzer, M. Edwards, S. Brandon, D. Clark, R. Town, C. Cerjan, R. Dylla-Spears, E. Mapoles, D. Munro, *et al.*, "Performance metrics for inertial confinement fusion implosions: Aspects of the technical framework for measuring progress in the National Ignition Campaign," Physics of Plasmas **19**, 056316 (2012).

[5] B. Cheng, T. J. Kwan, Y.-M. Wang, and S. H. Batha, "Scaling laws for ignition at the National Ignition Facility from first principles," Physical Review E **88**, 041101 (2013).

[6] J. Lindl, S. Haan, O. Landen, A. Christopherson, and R. Betti, "Progress toward a self-consistent set of 1d ignition capsule metrics in ICF," Physics of Plasmas **25**, 122704 (2018).

[7] O. Hurricane, P. Springer, P. Patel, D. Callahan, K. Baker, D. Casey, L. Divol, T. Döppner, D. Hinkel, M. Hohenberger, *et al.*, "Approaching a burning plasma on the NIF," Physics of Plasmas **26**, 052704 (2019).

[8] J. D. Lawson, "Some criteria for a power producing thermonuclear reactor," Proceedings of the Physical Society. Section B **70**, 6–10 (1957).

[9] R. Betti, P. Chang, B. Spears, K. Anderson, J. Edwards, M. Fatenejad, J. Lindl, R. McCrory, R. Nora, and D. Shvarts, "Thermonuclear ignition in inertial confinement fusion and comparison with magnetic confinement," Phys. Plasmas **17**, 058102 (2010).

[10] O. Hurricane, D. Callahan, D. Casey, E. Dewald, T. Dittrich, T. Döppner, S. Haan, D. Hinkel, L. B. Hopkins, O. Jones, *et al.*, "Inertially confined fusion plasmas dominated by alpha-particle self-heating," Nature Physics (2016).

[11] S. Le Pape, L. B. Hopkins, L. Divol, A. Pak, E. Dewald, S. Bhandarkar, L. Bennedetti, T. Bunn, J. Biener, J. Crippen, *et al.*, "Fusion energy output greater than the kinetic energy of an imploding shell at the National Ignition Facility," Physical Review Letters **120**, 245003 (2018).

[12] D. Clark, S. Haan, A. Cook, M. Edwards, B. Hammel, J. Koning, and M. Marinak, "Short-wavelength and three-dimensional instability evolution in National Ignition Facility ignition capsule designs," Physics of Plasmas **18**, 082701 (2011).

[13] P. Springer, O. Hurricane, J. Hammer, R. Betti, D. Callahan, E. Campbell, D. Casey, C. Cerjan, D. Cao, E. Dewald, *et al.*, "A 3D dynamic model to assess the impacts of low-mode asymmetry, aneurysms and mix-induced radiative loss on capsule performance across inertial confinement fusion platforms," Nuclear Fusion **59**, 032009 (2018).

[14] A. Zylstra and O. Hurricane, "On alpha-particle transport in inertial fusion," Physics of Plasmas **26**, 062701 (2019).

[15] H.-S. Bosch and G. Hale, "Improved formulas for fusion cross-sections and thermal reactivities," Nuclear Fusion **32**, 611 (1992).

[16] O. Hurricane, S. MacLaren, M. Rosen, J. H. Hammer, P. T. Springer, and R. Betti, "A thermodynamic condition for ignition and burn-propagation in cryogenic layer inertially confined fusion implosions," Physics of Plasmas **28**, 022704 (2021).

[17] G. Zimmerman and W. Kruer, "Numerical simulation of laser-initiated fusion," Comments Plasma Phys. Controlled Fusion **2**, 51–60 (1975).

[18] T. Dittrich, O. Hurricane, D. Callahan, E. Dewald, T. Döppner, D. Hinkel, L. B. Hopkins, S. Le Pape, T. Ma, J. Milovich, *et al.*, "Design of a high-foot high-adiabat ICF capsule for the National Ignition Facility," Physical Review Letters **112**, 055002 (2014).

[19] J. Paisner, E. Campbell, and W. Hogan, "The National Ignition Facility project," Fusion Technology **26**, 755–766 (1994).

[20] M. L. Spaeth, K. Manes, D. Kalantar, P. Miller, J. Heebner, E. Bliss, D. Spec, T. Parham, P. Whitman, P. Wegner, *et al.*, "Description of the NIF laser," Fusion Science and Technology **69**, 25–145 (2016).

[21] D. Wilson, P. Bradley, S. Goldman, N. Hoffman, R. Margevicius, R. Stephens, and R. Olson, "Developments in nif beryllium capsule design," Fusion Technology **38**, 16–21 (2000).

[22] E. Dewald, J. Pino, R. Tipton, J. Salmonson, J. Ralph, E. Hartouni, S. Khan, R. Hatarik, C. Young, D. Thorn, *et al.*, "Pushered single shell implosions for mix and radiation trapping studies using high-z layers on the National Ignition Facility," Physics of Plasmas **26**, 072705 (2019).

[23] S. Hu, R. Epstein, W. Theobald, H. Xu, H. Huang, V. Goncharov, S. Regan, P. McKenty, R. Betti, E. Campbell, *et al.*, "Direct-drive double-shell implosion: a platform for burning-plasma physics studies," Physical Review E **100**, 063204 (2019).

[24] S. W. Haan, M. Herrmann, T. Dittrich, A. Fetterman, M. Marinak, D. Munro, S. Pollaine, J. Salmonson, G. Strobel, and L. Suter, "Increasing robustness of indirect drive capsule designs against short wavelength hydrodynamic instabilities," Physics of Plasmas **12**, 056316 (2005).

[25] D. D.-M. Ho and S. MacLaren, Phys. Plasmas, in preparation (2021).

[26] E. Dewald, S. MacLaren, D. Martinez, R. Tipton, D. D.-M. Ho, and J. Pino, Phys. Plasmas, in preparation (2021).

[27] D. Hinkel, L. B. Hopkins, T. Ma, J. Ralph, F. Albert, L. Benedetti, P. Celliers, T. Döppner, C. Goyon, N. Izumi, *et al.*, "Development of improved radiation drive environment for high foot implosions at the National Ignition Facility," Physical review letters **117**, 225002 (2016).

[28] L. Pickworth, T. Döppner, D. Hinkel, J. Ralph, B. Bachmann, L. Masse, L. Divol, L. Benedetti, P. Celliers, H. Chen, *et al.*, "Application of cross-beam energy transfer to control drive symmetry in ICF implosions in low

gas fill hohlraums at the National Ignition Facility," Physics of Plasmas **27**, 102702 (2020).
[29]K. Baker, C. Thomas, D. Casey, M. Hohenberger, S. Khan, B. Spears, O. Landen, R. Nora, D. Woods, J. Milovich, *et al.*, "Hotspot parameter scaling with velocity and yield for high-adiabat layered implosions at the National Ignition Facility," Physical Review E **102**, 023210 (2020).
[30]D. Callahan, O. Hurricane, J. Ralph, C. Thomas, K. Baker, L. Benedetti, L. Berzak Hopkins, D. Casey, T. Chapman, C. Czajka, *et al.*, "Exploring the limits of case-to-capsule ratio, pulse length, and picket energy for symmetric hohlraum drive on the National Ignition Facility laser," Physics of Plasmas **25**, 056305 (2018).
[31]A. Zylstra, S. MacLaren, S. Yi, J. Kline, D. Callahan, O. Hurricane, B. Bachmann, G. Kyrala, L. Masse, P. Patel, *et al.*, "Implosion performance of subscale beryllium capsules on the NIF," Physics of Plasmas **26**, 052707 (2019).
[32]Y. Zhou, G. B. Zimmerman, and E. W. Burke, "Formulation of a two-scale transport scheme for the turbulent mix induced by Rayleigh-Taylor and Richtmyer-Meshkov instabilities," Physical Review E **65**, 056303 (2002).
[33]D. Callahan, O. Hurricane, D. Hinkel, T. Döppner, T. Ma, H.-S. Park, M. Barrios Garcia, L. Berzak Hopkins, D. Casey, C. Cerjan, *et al.*, "Higher velocity, high-foot implosions on the National Ignition Facility laser," Physics of Plasmas **22**, 056314 (2015).